*Article*

# The Structure and Location of 18-Crown-6 Ether in Zeolites RHO and ZK-5

Antony Nearchou [1,*], Catherine Dejoie [2], Paul R. Raithby [1] and Asel Sartbaeva [1,3,*]

1 Department of Chemistry, University of Bath, Claverton Down, Bath BA2 7AY, UK; chsprr@bath.ac.uk
2 European Synchrotron Radiation Facility, 71 Avenue des Martyrs, 38000 Grenoble, France; catherine.dejoie@esrf.fr
3 Centre for Sustainable and Circular Technologies, 1 South, University of Bath, Claverton Down, Bath BA2 7AY, UK
* Correspondence: a.nearchou@bham.ac.uk (A.N.); a.sartbaeva@bath.ac.uk (A.S.)

**Abstract:** The use of organic additives presents the greatest versatility and control of zeolite synthesis in order to prepare novel architectures for desired applications. Despite this prospect, there is little clarity of how organic additives are involved in framework assembly and the range of behaviours that are available. To address this issue, we have considered zeolites RHO and ZK-5 which can both be prepared using 18-crown-6 ether as an additive. Previously, this additive has shown to employ different structure directing behaviours to assemble a variety of zeolites. We have used high resolution powder X-ray diffraction and Rietveld refinement to determine structural models for zeolites RHO and ZK-5 with 18-crown-6 ether occluded in the framework. In doing so, we can observe the identity, location and orientation of the occluded additive and reason the structure directing behaviour in synthesis. We report that the isolated 18-crown-6 ether molecule is involved in the assembly of zeolite RHO, and for zeolite ZK-5 it is the $K^+$ coordinated macrocation. In both cases the relevant additive is disordered in the framework, suggesting that they behave as space-filling species that stabilise the formation of the $\alpha$-cage.

**Keywords:** zeolite; structure; crown-ether; rietveld refinement; occlusion; framework; cation; hydrothermal synthesis

## 1. Introduction

Zeolites are crystalline aluminosilicate minerals, known for their microporosity and pervasive use as molecular sieves, adsorbents and catalysts [1]. One of their most renowned uses is as catalysts for fluid catalytic cracking in the petrochemical industry [2]; however, there is ongoing research into using zeolites for hydrogen fuel storage [3], carbon dioxide capture [4] and selective extraction of radionuclides [5]. Their structure consists of a three-dimensional framework built from silica and alumina $TO_4$ tetrahedra (T = Si or Al) that are connected via a shared apical oxygen atom. Within the structure, it can be recognised that the $TO_4$ tetrahedra arrange themselves into regular geometric subunits, which are referred to as secondary building units (SBUs) [6].

Energetically, zeolites are recognised as being metastable and it is the stabilisation of the open framework cavities that is an integral factor dictating the crystallisation process. Species that provide such a structure stabilising effect are known as structure directing agents (SDAs) [7,8]. In natural occurring zeolite formation this stabilisation is achieved by metal cations which use electrostatic interactions to stabilise the voids and guide the assembly of certain SBUs [9]. For the preparation of synthetic zeolites, we can employ the use of organic additives that use a mixture of electrostatic, van der Waals and hydrogen-bonding interactions to direct structure [10–12]. Although the available non-bonding interactions between organic additives and the growing zeolite framework are known, there is little clarity on how exactly this impacts the zeolite crystallisation process. This

is particularly important if we are to rationally traverse the metastable zeolite synthesis landscape and prepare new zeolite architectures for intended applications. The prevalent use of organic additives is best illustrated by the fact that less than 30 of the 255 zeolitic frameworks recognised by the International Zeolite Association can be synthesised in the absence of an organic additive [13,14].

Davis and Lobo [15,16] suggest that the potential behaviour of organic additives can be divided into three classifications: true templates, organic structure directing agents (OSDAs) and space-filling species. True templates are seen to employ strong interactions and imprint their symmetry onto the growing framework. The discrepancy between OSDAs and templates is unclear, but the former is attributed by weaker interactions and an absence of symmetric or geometric matchup. Lastly, space-filling species are recognised by weak interactions and occupy the framework void spaces rather than being forthrightly involved in directing assembly. Despite these recognised categories, additional additive roles such as "structure-blocking" [17,18] and influence on the free-energy landscape of crystallisation [19,20] have been suggested but have received little research. Currently, computational calculations and synthetic approaches only consider the templating roles of organic species to rationally predict the ideal additives to prepare new zeolites [21–23]. However, a much wider appreciation of the structure directing capabilities of organic additives is required to take full advantage of their use in zeolite design.

18-crown-6 ether (18C6) is an example of an organic additive that can be used in the synthesis of multiple zeolites with a variety of topologies [24–27]. Previously, it has been observed that 18C6 can undertake differing roles in the synthesis of the polymorphic **EMT** and **FAU**-type zeolites. [20,28] Although in both the 18C6 exists as a ((18C6)Na$^+$) macrocation, it is a true geometric template for the synthesis of **EMT**-type zeolites and a space-filling species in the synthesis of **FAU**-type zeolites [29–33]. This is important, as it demonstrates the integral role of 18C6 in the synthesis mechanism to differentiate between the two polymorphs. Zeolites RHO and ZK-5 (**KFI**) are two zeolites that can also be prepared using 18C6 [24,26]; however, the role, identity, and location of the 18C6 species has not been determined. Figure 1 shows the framework structure of these two zeolites, in addition to the constituent SBUs. Both zeolites consist of α-cages in a body-centred cubic arrangement and it is these α-cages that the 18C6 is believed to occupy [33,34]; however, this has not been explicitly proven. Due to the lack of structural information, there is currently no understanding of how the 18C6 molecule is involved in the synthesis of these two zeolites in comparison to the **FAU** and **EMT**-type zeolites.
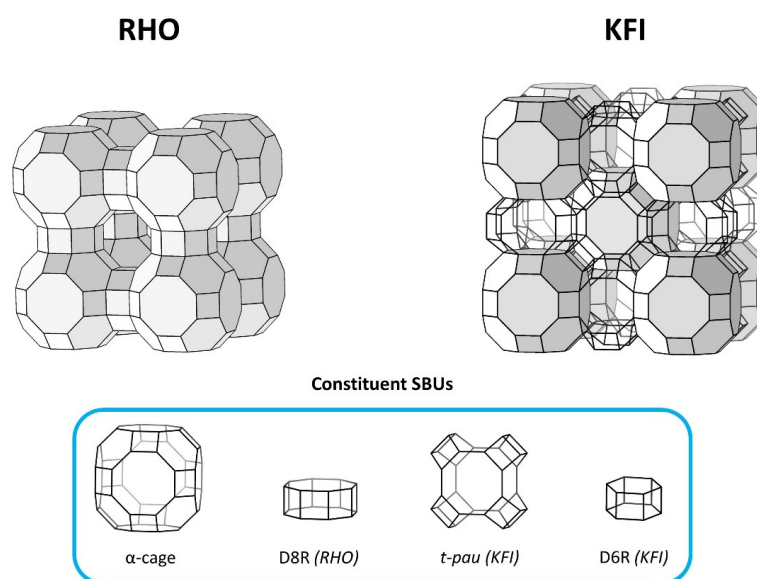


**Figure 1.** Structure of the **RHO** and **KFI** framework types. Included are the constituent SBUs: the α-cage, the double 8-ring (D8R), *t-pau* unit and the double 6-ring (D6R). For the latter three the code in

parenthesis indicates the framework that this SBU belongs to exclusively. The framework structures are shown with the α-cages and D8Rs as solid polyhedra.

For the first time, we report the crystal structure of zeolites RHO and ZK-5 with the 18C6 species occluded within their zeolite frameworks. We present experimental evidence that the 18C6 molecule occupies the α-cage cavities in both zeolites, in addition to the cation the molecule is coordinated to. Using these structures, we have gleaned the role of the 18C6 organic additive throughout the crystallisation of both zeolites.

## 2. Methods

### 2.1. Sample Preparation

The zeolite RHO and ZK-5 samples were synthesised using the verified procedures reported by Chatelain et al. [24,26,27,34] using 18-crown-6 ether (18C6) as organic additive. The molar batch compositions used in the synthesis of each zeolite are shown in Table 1. The materials used for sample preparation were sodium hydroxide (NaOH), potassium hydroxide (KOH), strontium nitrate ($Sr(NO_3)_2$), caesium hydroxide solution (50 wt% CsOH in water), 18-crown-6 ether ($C_{12}H_{24}O_6$, 18C6), sodium aluminate ($NaAlO_2$), aluminium hydroxide ($Al(OH)_3$), colloidal silica (LUDOX® HS-40, 40 wt% $SiO_2$ in water) and deionised water. Aside from the deionised water, all the materials used were purchased from Sigma-Aldrich (Gillingham, UK).

**Table 1.** Hydrogel batch compositions used to prepare zeolites RHO and ZK-5.

| Zeolite | $Al_2O_3$ | $Na_2O$ | $K_2O$ | SrO | $Cs_2O$ | $SiO_2$ | 18C6 | $H_2O$ |
|---------|-----------|---------|--------|-----|---------|---------|------|--------|
| RHO | 1 | 1.8 | | | 0.3 | 10 | 0.50 | 100 |
| ZK-5 | 1 | | 2.7 | 0.1 | | 10 | 1.0 | 220 |

### 2.2. Zeolite RHO

Zeolite RHO was prepared as follows. First, the sodium and caesium hydroxide were added to the deionised water, followed by the addition of the 18C6. Upon complete dissolution the sodium aluminate was added, and the mixture permitted to stir until it was homogeneous. Next the colloidal silica was slowly poured into the solution under stirring, to negate any rapid gelation. The produced hydrogel was then aged under stirring at ambient conditions for 24 h. After aging, the hydrogel was transferred to a Teflon cup within a stainless-steel autoclave and heated at 110 °C for 8 days. Following heating, the autoclave was removed from the oven and left to cool to ambient temperature. The crystallised zeolite product was subsequently separated from the mother liquor via Buchner filtration and washed with deionised water until the pH of the filtrate was neutral. The product was then dried at 90 °C, before being ground prior to further calcination and dehydration.

### 2.3. Zeolite ZK-5

The zeolite ZK-5 precursor hydrogel was prepared by first dissolving the potassium hydroxide in a portion of the deionised water. The aluminium hydroxide was added to this solution, and then dissolved under stirring and heating to near 110 °C. After dissolution, the solution was cooled to ambient temperature and replenished with any water loss via evaporation during heating. In a separate vessel the 18C6 and strontium nitrate were dissolved in the second portion of deionised water. The colloidal silica was then poured into this solution and stirred until homogeneous. Next, the previously prepared alumina solution was rapidly poured into the silica solution under stirring to produce the hydrogel, which was aged under stirring for 30 min. After aging, the hydrogel was transferred to a Teflon cup within a stainless-steel autoclave and heated at 150 °C for 5 days. Following heating, the autoclave was removed from the oven and cooled to ambient temperature. To

retrieve the as-synthesised zeolite ZK-5 sample the same process of separation, washing and drying performed for zeolite RHO was used.

## 2.4. Calcination and Dehydration

The as-synthesised sample of each zeolite was divided into two halves, to produce the filled and empty analogues. The filled analogue was synthesised with the 18C6 intact, and the empty analogue was calcined to remove the occluded 18C6.

Calcination was achieved by heating the relevant analogue in a tube furnace under air to 450 °C for 6 h at a ramp rate of 1 °C·min$^{-1}$. Throughout this heating cycle the temperature was held static at 100 °C, 200 °C and 300 °C for 1 h each. After calcination the sample was cooled at a rate of 1°C·min$^{-1}$ to ambient conditions, including a static stage at 200 °C for 1 h.

Based on sample conditions on the respective diffractometers, only the zeolite RHO empty and filled samples were dehydrated in preparation for measurements. This was performed by heating the samples in a tube furnace under vacuum. The heating cycle consisted of a ramp rate of 1°C·min$^{-1}$, with static temperatures stages of 100 °C for 1 h and 200 °C for 6 h. Following this, the sample was then cooled to ambient conditions at a rate of 1 °C·min$^{-1}$, including a static stage at 100 °C for 1 h during this cooling cycle. The dehydrated sample was then transferred under vacuum to a dry argon glove box and sealed into a glass vial under argon gas.

## 2.5. Thermogravimetry

The 18C6 and water mass content of the empty and filled zeolite analogues were studied using thermogravimetry. This was conducted on samples which had not been dehydrated. A Setaram Setsys Evolution TGA 16/18 (KEP Technologies Group, Sophia Antipolis, France) was used, with samples loaded into open 170 μL alumina crucibles. The samples were heated from 30 °C to 600 °C at a ramp rate of 5 °C·min$^{-1}$, under 20 mL·min$^{-1}$ flow of air. Instrumental errors were accounted for by correcting with a thermogravimetric scan of an empty crucible.

## 2.6. Elemental Analysis

The framework Si/Al ratio was estimated by using both energy dispersive X-ray (EDX) spectroscopy and solid-state magic angle spinning (SS MAS) nuclear magnetic resonance (NMR) spectroscopy.

EDX spectroscopy was performed using an Oxford INCA X-ray analyser (Oxford Instruments, Abingdon, UK) equipped to a JEOL SEM6480LV microscope (JEOL GmbH, Freising, Germany). Multiple sites on a variety of crystals were analysed, with an average and standard deviation recorded. The spectral line intensities measured were compared to a calibration standard.

SS MAS NMR spectroscopy of the $^{29}$Si nuclei was performed at the formerly EPSRC-sponsored SS NMR service at Durham University (Durham, UK). A Varian VNMRS spectrometer (Varian Inc., Palo Alto, CA, USA) was used, operating with a 9.4 T magnet, and equipped with two magic-angle spinning probes. Neat Si(CH$_3$)$_4$ was used as a chemical shift reference. Measurements were taken under an inert nitrogen atmosphere, with direct excitations using a frequency of 79.435 MHz, a pulse duration of 4.0 μs, a 5000 Hz spin rate and a 20.0 ms acquisition time. $^1$H cross-polarisation was performed at the same conditions, with the addition of two-pulse phase-modulated decoupling frequencies of 40 and 55 kHz. From this it was seen that there was a negligible concentration of Si-OH silanols present. The Si/Al ratio was determined using the conventional method of Lippmaa et al. [35].

## 2.7. High Resolution Powder X-ray Diffraction

Both the empty and filled analogues of zeolites RHO and ZK-5 were analysed using high-resolution powder X-ray diffraction. The diffraction patterns for the dehydrated zeolite RHO samples were recorded on the ID22 beamline at the European Synchrotron

Radiation Facility (ESRF) in Grenoble, France. The detector parameters were calibrated with silicon and the incident X-ray radiation had a wavelength of 0.49598 Å. The samples were loaded into 1 mm diameter borosilicate capillaries within an inert nitrogen atmosphere to prevent any sample hydration. The capillaries were subsequently sealed with vacuum grease and wax, before being mounted onto the diffractometer and cooled to 100 K using an Oxford Cryosystems Cryostream 700 Plus. (Oxford Cryosystems, Oxford, UK). A scan range of 2θ = 0.5–45.0° (binning size of 0.002°) was used, equating to a scan length of approximately 22 min. Throughout scanning the capillaries were spun perpendicular to the X-ray beam to reduce preferred orientation effects.

The hydrated zeolite ZK-5 samples were analysed using a STOE STADI MP diffractometer (STOE & Cie GmbH, Darmstadt, Germany), equipped with a MYTHEN2 1K silicon strip detector (Dectris AG, Baden-Daettwil, Switzerland). The incident X-ray radiation was pure Cu Kα1, of wavelength 1.5406 Å, obtained using a Cu X-ray tube and a Ge(111) monochromator. A scan range of 2θ = 3–100°, step size of 0.015° and scan length of 13.6 h were used. The diffraction measurements were obtained in the Debye–Scherrer mode, using a transmission sample holder between two foil insets with 3 mm masks. The diffraction patterns were recorded at ambient temperature.

The patterns obtained from both diffractometers were used for structure determination, using the Rietveld method in the TOPAS Academic software (Coelho Software, Brisbane, Australia) [36]. The starting structures used were the crystal structures of zeolite RHO in the $I\bar{4}3m$ symmetry and the synthetic (Cs, K)-ZK5 zeolite, both reported by Parise et al. [37,38]. For the latter ZK5 zeolite structure, the Cs sites were substituted with K sites prior to the refinement process. First the structure of the empty analogues of zeolites RHO and ZK-5 were determined, and these models used as the starting structures for the respective filled analogues.

The Rietveld refinements were performed using the 2θ = 2.0–45.0° and 2θ = 5.0–100.0° data ranges for the zeolite RHO and ZK-5 samples accordingly. During the refinement process 100,000 iterations were used, in addition to a $\chi^2$ convergence criteria of 0.001. The quality of the Rietveld fit was evaluated using the goodness of fit factor $G$, equal to $R_{wp}/R_{exp}$. [39] The average mean-square displacement in all directions, $B_{eq}$, was used to assess the degree of atomic displacement [40]. The 18C6 oxyethylene chain was modelled as a rigid body, using the Cartesian coordinates of a geometry-optimised 18C6 species used previously by Nearchou et al. [33]. The occupancy of the C and O oxyethylene chain sites were constrained to be equivalent, and translations and rotations of the rigid body refined. A summary of the refinement process and profile functions are included in the Supplementary Materials.

## 3. Results

### 3.1. Initial Characterisation

The samples were first characterised to aid the starting models in the refinement process. The results obtained are shown in Table 2. The Si/Al ratio of the zeolite RHO and ZK-5 samples were estimated at 3.8 and 4.0, respectively, which both agree with the observations of Chatelain et al. [34]. The zeolite samples were analysed using thermogravimetry, with the thermogravimetric curves shown in Figures S1 and S2 in the supporting information (SI). The filled zeolites exhibit distinct dehydration and 18C6 decomposition events at different temperatures. The mass% content of 18C6 was estimated at 7.3% and 2.9% for zeolites RHO and ZK-5, respectively, agreeing with our previous observations [41]. Using these mass% contents, it is calculated that for both zeolites there is approximately one 18C6 molecule per unit cell. The absence of a 18C6 decomposition step for the empty zeolite analogues confirms that the 18C6 has successfully been removed. Furthermore, previous inelastic neutron scattering spectroscopy of these samples has demonstrated that the 18C6 oxyethylene chain is intact in the filled analogues, due to the presence of the fingerprint vibrational modes [33].

**Table 2.** The estimated Si/Al ratio of the filled zeolite samples, as estimated by $^{29}$Si SS MAS NMR and EDX spectroscopy. Included is the estimated mass% content of 18C6 and water. Error in parentheses.

| | Si/Al Ratio | | TGA–Mass% | |
| --- | --- | --- | --- | --- |
| | $^{29}$**Si NMR** | **EDX** | **18C6** | **Water** |
| Zeolite RHO | 3.93 | 3.7(2) | 7.3(1) | 9.9(2) |
| Zeolite ZK-5 | | 4.0(1) | 2.9(1) | 11.5(1) |

*3.2. Zeolite RHO*

The powder X-ray diffraction patterns and final Rietveld fits for both the empty and filled zeolite RHO samples are shown in Figure 2. These figures also include the goodness of fit *G* value for the Rietveld fits, as well as the difference between the experimental data and the fit. The lowest-angle Bragg peak corresponding to the Miller index (110) is shown in a separate plot for ease of visualisation, due to the intensity being an order of magnitude greater than the other peaks in the diffraction pattern. Tables 3 and 4 contain the final refined unit cell parameters and crystallographic data for the empty and filled zeolites accordingly. Both zeolites were fit using the *I*$\bar{4}$3*m* space group as opposed to the ambient higher symmetry *Im*$\bar{3}$*m* space group that zeolite RHO is typically reported in [42,43], as shown in Figure 1. However, there is substantial evidence in the literature where the symmetry is lowered due to certain stimuli, such as dehydration [36] and low temperatures [44] which are relevant here, as well as applying mechanical pressure [45,46]. The *I*$\bar{4}$3*m* symmetry is characterised by elliptical deformations in the eight-ring apertures, as illustrated in Figure 3.
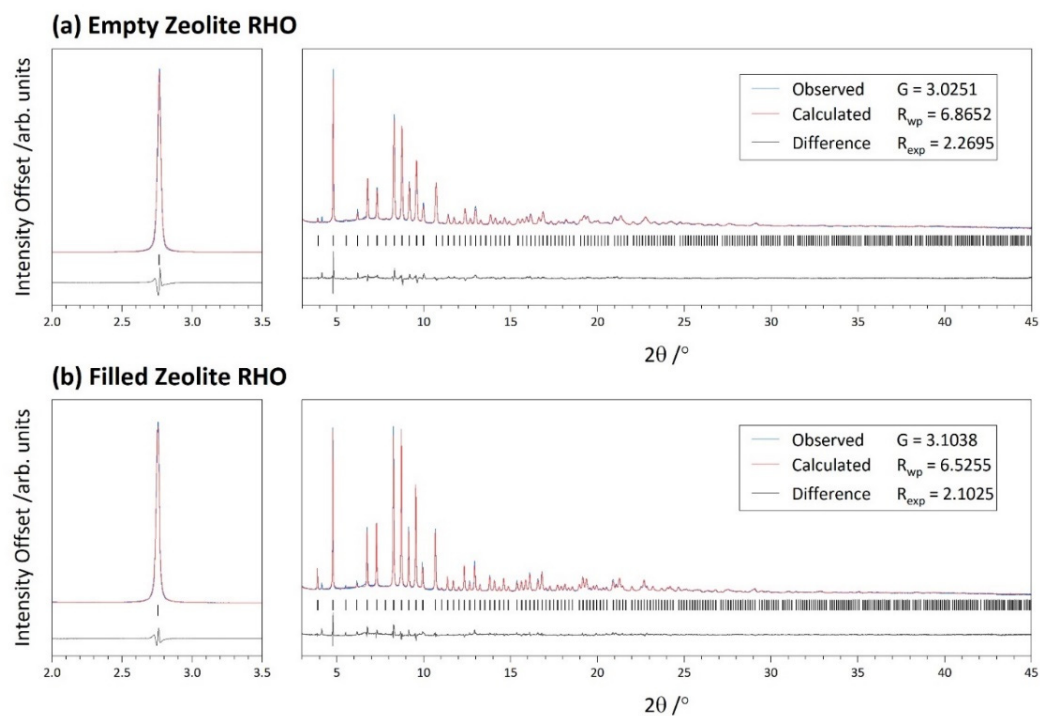


**Figure 2.** Powder X-ray diffraction patterns for the (**a**) empty and (**b**) filled zeolite RHO samples. The experimental data are shown in blue, the Rietveld fit in red and the difference between the two in grey. Included is the 2θ = 3.0–45.0° range (**right**) and an insert of the 2θ = 2.0–3.5° range (**left**) covering the (110) Bragg peak. The incident X-ray radiation wavelength was 0.49598 Å.

**Table 3.** Final refined unit cell parameters and crystallographic sites for the empty zeolite RHO sample. 'Occ.' refers to the fractional occupancy of the relevant crystallographic site. Error in parentheses.

| Symmetry | | Unit Cell | | Refinement | |
|---|---|---|---|---|---|
| **Cubic** | | *a*/Å | **14.5450(1)** | G | 3.0251 |
| $I\bar{4}3m$ | | | | $R_{wp}$ | 6.8652 |
| | | | | $R_{exp}$ | 2.2695 |
| Atom | *x* | *y* | *z* | Occ. | $B_{eq}$ |
| Si | 0.2702(1) | 0.1220(1) | 0.4217(1) | 0.78(2) | 0.27(2) |
| Al | 0.2702(1) | 0.1220(1) | 0.4217(1) | 0.22(2) | 0.27(2) |
| O(1) | 0.2134(2) | 0.2134(2) | 0.3962(3) | 1 | 0.98(4) |
| O(2) | 0.1264(2) | 0.1264(2) | 0.6238(2) | 1 | 0.98(4) |
| O(3) | 0.0326(2) | 0.2055(2) | 0.3858(2) | 1 | 0.98(4) |
| Cs | 0 | 0 | 0.5 | 0.619(1) | 4.81(4) |
| Na | 0.3333 | 0.3333 | 0.3333 | 0.220(6) | 2.0(5) |

**Table 4.** Final refined unit cell parameters and crystallographic sites for the filled zeolite RHO sample. 'Occ.' refers to the fractional occupancy of the relevant crystallographic site. Error in parentheses.

| Symmetry | | Unit Cell | | Refinement | |
|---|---|---|---|---|---|
| **Cubic** | | *a*/Å | **14.58787(5)** | G | 3.1038 |
| $I\bar{4}3m$ | | | | $R_{wp}$ | 6.5255 |
| | | | | $R_{exp}$ | 2.1025 |
| Atom | *x* | *y* | *z* | Occ. | $B_{eq}$ |
| Si | 0.2704(1) | 0.1210(1) | 0.4215(1) | 0.78(2) | 0.31(2) |
| Al | 0.2704(1) | 0.1210(1) | 0.4215(1) | 0.22(2) | 0.31(2) |
| O(1) | 0.2127(1) | 0.2127(1) | 0.4005(2) | 1 | 0.70(3) |
| O(2) | 0.1274(1) | 0.1274(1) | 0.6254(2) | 1 | 0.70(3) |
| O(3) | 0.0287(1) | 0.2105(1) | 0.3853(1) | 1 | 0.70(3) |
| Cs | 0 | 0 | 0.5 | 0.697(1) | 4.79(3) |
| Na | 0.3132(6) | 0.3132(6) | 0.3132(6) | 0.229(5) | 1.4(4) |
| C(1) | 0.2215(1) | 0.0577(1) | 0.1020(1) | 0.0227(1) | 3.7(6) |
| C(2) | 0.1818(1) | −0.0072(1) | 0.1724(1) | 0.0227(1) | 3.7(6) |
| C(3) | 0.0416(1) | −0.0530(1) | 0.2415(1) | 0.0227(1) | 3.7(6) |
| C(4) | −0.0605(1) | −0.0343(1) | 0.2409(1) | 0.0227(1) | 3.7(6) |
| C(5) | −0.1945(1) | −0.0510(1) | 0.1498(1) | 0.0227(1) | 3.7(6) |
| C(6) | −0.2279(1) | −0.0867(1) | 0.0582(1) | 0.0227(1) | 3.7(6) |
| C(7) | 0.2279(1) | 0.0867(1) | −0.0582(1) | 0.0227(1) | 3.7(6) |
| C(8) | −0.2215(1) | −0.0577(1) | −0.1020(1) | 0.0227(1) | 3.7(6) |
| C(9) | 0.1945(1) | 0.0510(1) | −0.1498(1) | 0.0227(1) | 3.7(6) |
| C(10) | 0.0605(1) | 0.0343(1) | −0.2409(1) | 0.0227(1) | 3.7(6) |
| C(11) | −0.0416(1) | 0.0530(1) | −0.2415(1) | 0.0227(1) | 3.7(6) |
| C(12) | −0.1818(1) | 0.0072(1) | −0.1724(1) | 0.0227(1) | 3.7(6) |
| O(4) | 0.1898(1) | 0.0320(1) | 0.0132(1) | 0.0227(1) | 3.7(6) |
| O(5) | 0.0846(1) | 0.0024(1) | 0.1734(1) | 0.0227(1) | 3.7(6) |
| O(6) | −0.0976(1) | −0.0618(1) | 0.1547(1) | 0.0227(1) | 3.7(6) |
| O(7) | −0.1898(1) | −0.0320(1) | −0.0132(1) | 0.0227(1) | 3.7(6) |
| O(8) | 0.0976(1) | 0.0618(1) | −0.1547(1) | 0.0227(1) | 3.7(6) |
| O(9) | −0.0846(1) | −0.0024(1) | −0.1734(1) | 0.0227(1) | 3.7(6) |
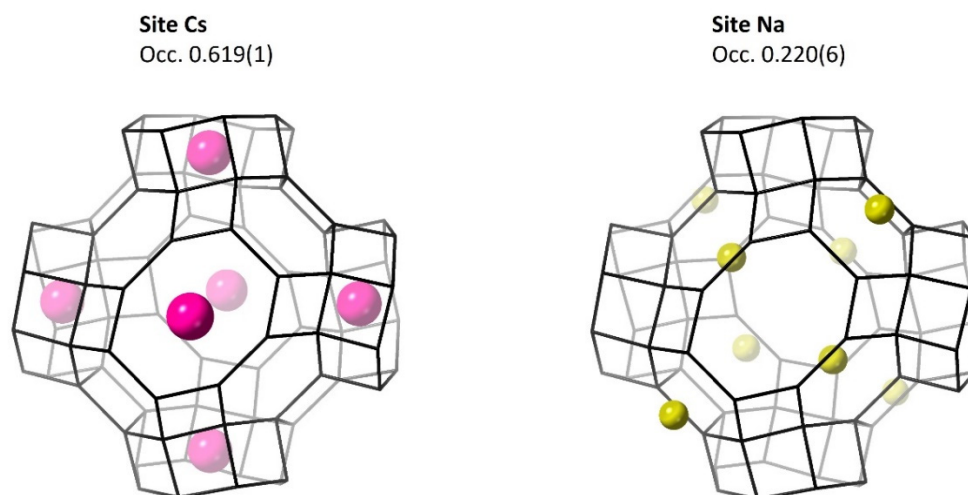
**Figure 3.** Location of the Cs and Na cation sites determined in the empty zeolite RHO. The framework is shown as a stick model, the caesium cations as pink spheres and the sodium cations in yellow. The fractional occupancy (Occ.) of each site is also included.

### 3.2.1. Metal Cations

Two crystallographic metal cation sites were determined in both zeolite RHO structures—these being a Cs$^+$ and a Na$^+$ site. Both cation sites are at special positions in the structure and are shown in Figure 3 for the empty zeolite. The Cs site is positioned at the centre of the distorted double eight-ring (D8R) units, between the elliptical eight-ring apertures. Alternatively, the Na site is associated with the single six-ring (S6R) faces of the α-cage. The Na sites are located within the interior of an α-cage if the associated S6R face is connected to the minor axis of the elliptical eight-ring aperture. Both cation sites are comparable to those reported by Robson et al. [43] in the ambient $Im\overline{3}m$ space group, despite the difference in symmetry. The only distinctions are that in the Robson structure the Cs site is located in the centre of each eight-ring aperture, and a Na site is observed on either side of the S6R faces. Both cation sites are observed in the filled zeolite RHO structure; however, the Na site is observed to move closer to the S6R faces of the α-cage. This is likely due to the occlusion of the 18C6 species.

### 3.2.2. The 18C6 Species

The occluded 18C6 species was modelled as a rigid body within the zeolite RHO structure, occupying the framework α-cage as is suspected [33,34]. Figure 4 shows the structure of the 18C6 species within the α-cage. During the refinement process no cations were observed to occupy the centre of the 18C6 cavity, in contrast to the ((18C6)Na$^+$) macrocation seen in zeolite EMC-2 (**EMT**) by Baerlocher et al. [29]. This suggests that during crystallisation, it is the isolated 18C6 molecule, as opposed to a macrocation complex with a central Na$^+$ or Cs$^+$ cation, that is involved in the assembly of the **RHO** framework. However, the interatomic distance between the Na site and site O(8) of the oxyethylene chain is 2.29 Å, which is within the expected range of a Na-O bond [47]. This suggests that although the 18C6 molecule is not coordinated to a central cation in its cavity, it is coordinated to a Na cation that is also electrostatically associated with the zeolite framework.

Due to the body-centred symmetry of the structure, each C and O site has a multiplicity of 48 within the unit cell, and 24 within the α-cage. As the occupancy of the C and O sites were constrained to be equivalent, the occupancy of the rigid body 18C6 species was refined to 0.0227(1). Considering the occupancy and multiplicity of the crystallographic sites, it is estimated that there are 1.1 18C6 molecules per unit cell, which is congruent with the thermogravimetric analysis. Furthermore, this is equivalent to 0.54 18C6 molecules per α-cage. The cubic crystal symmetry results in several orientations of the 18C6 species, with two examples shown in Figure 4. The 18C6 molecules is not aligned to a single

crystallographic axis, and there does not appear to be any periodic ordering in orientations of the 18C6 species between unit cells. Therefore, the refined structure is an average of the different permutations of 18C6 orientations available. These observations are in contrary to zeolite EMC-2 [29], where the 18C6 species is observed exclusively in the *ab* plane and is congruent with the six-fold hexagonal symmetry of the **EMT** framework.
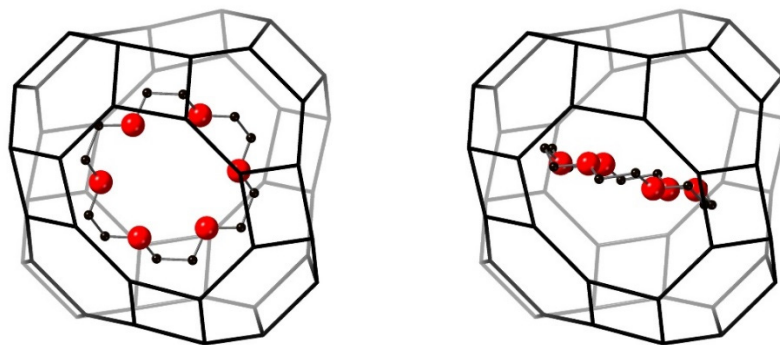


**Figure 4.** Location of the C and O sites of the 18C6 oxyethylene chain in the α-cage of the filled zeolite RHO. An example of two 18C6 orientations in the cage are shown. The framework is shown as a stick model, the carbon sites as black spheres and the oxygen sites as red spheres.

*3.3. Zeolite ZK-5*

Figure 5 shows the powder X-ray diffraction patterns and final Rietveld fits for the hydrated empty and filled zeolite ZK-5 samples accordingly. Included is a plot of the difference between the experimental data and the fit, in addition to the model's goodness of fit *G* value. The final refined crystallographic coordinates and unit cell parameters for the empty and filled samples are displayed in Tables 5 and 6, respectively. Both zeolites were fit using the $Im\bar{3}m$ space group, which is the ambient symmetry anticipated for zeolite ZK-5 [38,45,47]. The phase purity of the empty sample was calculated as 90.2% zeolite ZK-5 and 9.8% zeolite W. For the filled sample this was 88.9% and 11.1% for ZK-5 and W, respectively.

**Table 5.** Final refined unit cell parameters and crystallographic sites for the empty zeolite ZK-5 sample. 'Occ.' refers to the fractional occupancy of the relevant crystallographic site. Error in parentheses.

| Symmetry | | Unit Cell | | Refinement | |
|---|---|---|---|---|---|
| **Cubic** | | *a*/Å | **18.6816(1)** | G | 4.0775 |
| $Im\bar{3}m$ | | | | $R_{wp}$ | 6.9525 |
| | | | | $R_{exp}$ | 1.7051 |
| Atom | *x* | *y* | *z* | Occ. | $B_{eq}$ |
| Si | 0.0835(1) | 0.2014(1) | 0.3189(1) | 0.82(3) | 0.26(4) |
| Al | 0.0835(1) | 0.2014(1) | 0.3189(1) | 0.18(3) | 0.26(4) |
| O(1) | 0.1269(2) | 0.1269(2) | 0.3119(3) | 1 | 0.46(7) |
| O(2) | 0.2550(2) | 0.2550(2) | 0.4080(3) | 1 | 0.46(7) |
| O(3) | 0 | 0.1860(3) | 0.3329(3) | 1 | 0.46(7) |
| O(4) | 0.25 | 0.1124(2) | 0.3876(2) | 1 | 0.46(7) |
| K(1) | 0 | 0.25 | 0.5 | 1.000(6) | 3.2(1)) |
| K(2) | 0.15 | 0.15 | 0.15 | 0.352(5) | 3.2(1) |
| K(3) | 0 | 0 | 0.3588(7) | 0.402(6) | 3.2(1) |
| Ow(1) | 0.0931(5) | 0 | 0.5 | 1.000(6 | 18.0(5) |
| Ow(2) | 0.3333 | 0.4256(5) | 0.5 | 0.646(3) | 18.0(5) |
| Ow(3) | 0.1208(6) | 0.1208(6) | 0.1208(6) | 0.648(5) | 18.0(5) |
| Ow(4) | 0 | 0 | 0.300(2) | 0.57(1) | 18.0(5) |

**Table 6.** Final refined unit cell parameters and crystallographic sites for the filled zeolite ZK-5 sample. 'Occ.' refers to the fractional occupancy of the relevant crystallographic site. Error in parentheses.

| Symmetry | | Unit Cell | | Refinement | |
|---|---|---|---|---|---|
| **Cubic** | | *a*/Å | **18.68867(7)** | G | 3.9496 |
| $Im\bar{3}m$ | | | | $R_{wp}$ | 7.0177 |
| | | | | $R_{exp}$ | 1.7768 |
| Atom | *x* | *y* | *z* | Occ. | $B_{eq}$ |
| Si | 0.0834(1) | 0.2019(1) | 0.3209(1) | 0.79(2) | 0.74(4) |
| Al | 0.0834(1) | 0.2019(1) | 0.3209(1) | 0.21(2) | 0.74(4) |
| O(1) | 0.1286(2) | 0.1286(2) | 0.3142(3) | 1 | 1.10(7) |
| O(2) | 0.2547(2) | 0.2547(2) | 0.4090(2) | 1 | 1.10(7) |
| O(3) | 0 | 0.1852(3) | 0.3329(3) | 1 | 1.10(7) |
| O(4) | 0.25 | 0.1115(2) | 0.3885(2) | 1 | 1.10(7) |
| K(1) | 0 | 0.25 | 0.5 | 1.000(4) | 4.4(1) |
| K(3) | 0 | 0 | 0.415(1) | 0.243(7) | 4.4(1) |
| Ow(1) | 01082(5) | 0 | 0.5 | 0.866(9) | 7.4(3) |
| Ow(3) | 0.1386(4) | 0.1386(4) | 0.1386(4) | 1.00(2) | 7.4(3) |
| Ow(4) | 0 | 0 | 0.3317(8) | 0.96(1) | 7.4(3) |
| C(1) | 0.0318(1) | 0.0431(1) | 0.1882(1) | 0.0276(2) | 15.5(8) |
| C(2) | −0.0211(1) | −0.0180(1) | 0.1937(1) | 0.0276(2) | 15.5(8) |
| C(3) | −0.1221(1) | −0.0695(1) | 0.1362(1) | 0.0276(2) | 15.5(8) |
| C(4) | −0.1714(1) | −0.0605(1) | 0.0725(1) | 0.0276(2) | 15.5(8) |
| C(5) | −0.1750(1) | −0.0688(1) | 0.0543(1) | 0.0276(2) | 15.5(8) |
| C(6) | −0.1293(1) | −0.0862(1) | 0.1189(1) | 0.0276(2) | 15.5(8) |
| C(7) | 0.1293(1) | 0.0862(1) | 0.1189(1) | 0.0276(2) | 15.5(8) |
| C(8) | −0.0318(1) | −0.0431(1) | −0.1882(1) | 0.0276(2) | 15.5(8) |
| C(9) | 0.1750(1) | 0.0688(1) | 0.0543(1) | 0.0276(2) | 15.5(8) |
| C(10) | 0.1714(1) | 0.0605(1) | −0.0725(1) | 0.0276(2) | 15.5(8) |
| C(11) | 0.1221(1) | 0.0695(1) | −0.1362(1) | 0.0276(2) | 15.5(8) |
| C(12) | 0.0211(1) | 0.0180(1) | −0.1937(1) | 0.0276(2) | 15.5(8) |
| K(4) | 0 | 0 | 0 | 0.653(9) | 4.4(1) |
| O(5) | 0.0752(1) | 0.0330(1) | 0.1263(1) | 0.0276(2) | 15.5(8) |
| O(6) | −0.0679(1) | −0.0159(1) | 0.1335(1) | 0.0276(2) | 15.5(8) |
| O(7) | −0.1318(1) | −0.0725(1) | 0.0084(1) | 0.0276(2) | 15.5(8) |
| O(8) | −0.0752(1) | −0.0330(1) | −0.1263(1) | 0.0276(2) | 15.5(8) |
| O(9) | 0.1318(1) | 0.0725(1) | −0.0084(1) | 0.0276(2) | 15.5(8) |
| O(10) | 0.0679(1) | 0.0159(1) | −0.1335(1) | 0.0276(2) | 15.5(8) |

### 3.3.1. Metal Cations

Three crystallographic K$^+$ cation sites were determined in the structure of the empty zeolite ZK-5 and are shown in Figure 6. The first of these is the K(1) site located in the puckered eight-ring opening that links two adjoining orthogonal *t-pau* units. The site has an occupancy of 1.000(6), which the literature has shown to consistently be the most energetically favourable and highest-population cation site in **KFI**-type zeolites [38,48–50]. It is this observation that strongly suggests that the K$^+$ cations play an active role in directing these puckered eight-ring openings, and consequently the **KFI** framework, during crystallisation. The K(2) site is located in the interior of the α-cage adjacent to the S6R faces, which adjoin the double six-ring (D6R) units between α-cages, with an occupancy of 0.352(5). Lastly, the K(3) site has an occupancy of 0.402(6) and is positioned within the *t-pau* units but associated with the single eight-ring (S8R) apertures that connect to the α-cage. All three of these cation sites are congruent with those observed for the (Cs,K)-ZK5 zeolite by Parise et al. [38] with the distinction that the Cs site is occupied by the K(3) site herein. These sites also agree with the crystal structure reported by Lievens et al. [49] for zeolite

ZK-5. It should be noted that for the structure herein the D6R units are vacant of $K^+$ cations, consistent with calculations by Lievens et al. that this site has a high energy in the **KFI** framework and is unfavourable to occupy.
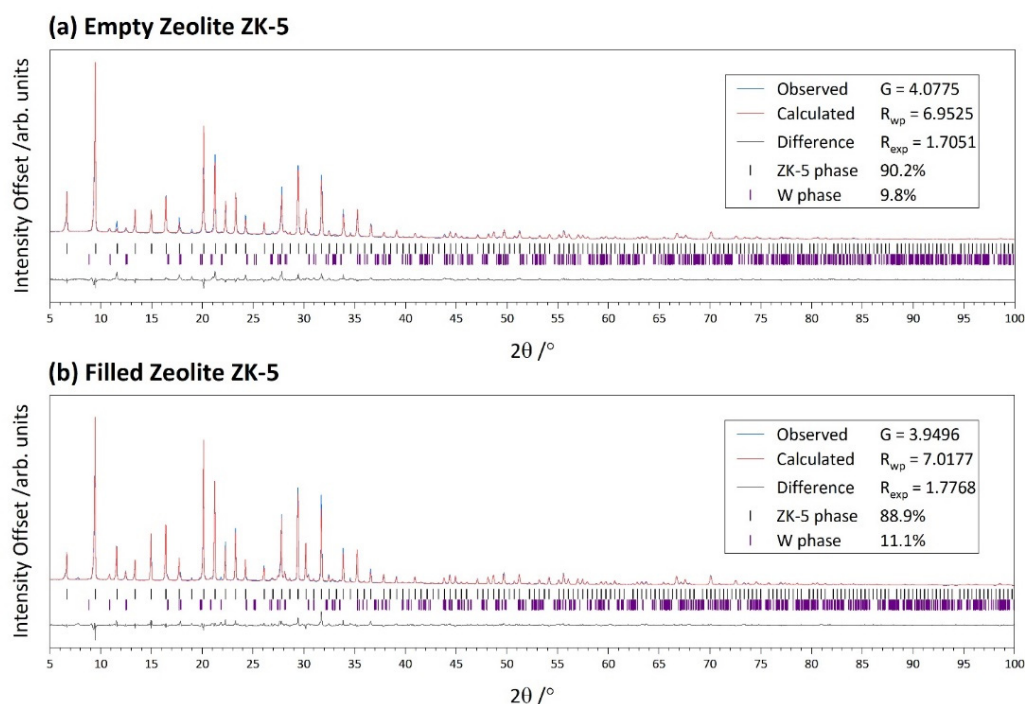
**(a) Empty Zeolite ZK-5**



**(b) Filled Zeolite ZK-5**



**Figure 5.** Powder X-ray diffraction patterns for the (**a**) empty and (**b**) filled zeolite ZK-5 samples. The experimental data are shown in blue, the Rietveld fit in red and the difference between the two in grey. Bars in black indicate Bragg peaks belonging to the ZK-5 phase, and purple to the impurity W phase. The incident X-ray radiation wavelength was 1.5406 Å.

**Site K(1)**
Occ. 1.000(6)

**Site K(2)**
Occ. 0.352(5)

**Site K(3)**
Occ. 0.402(6)
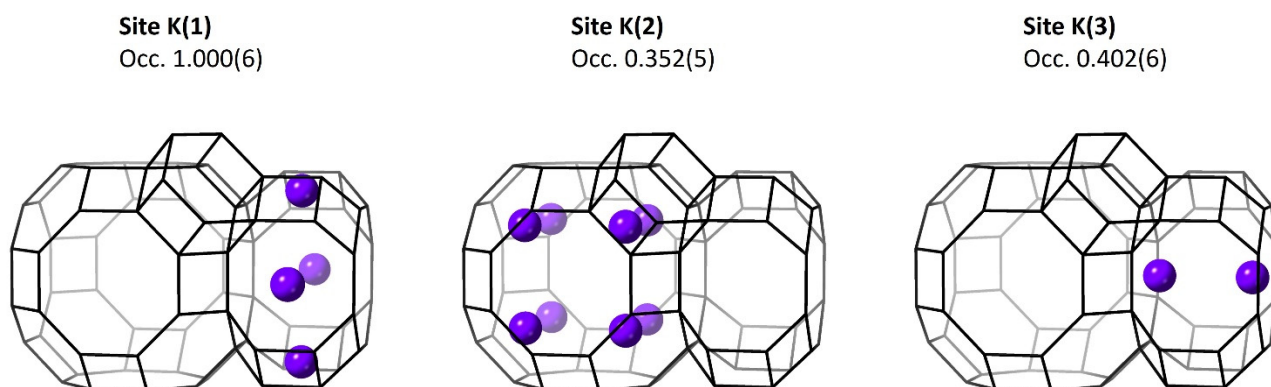


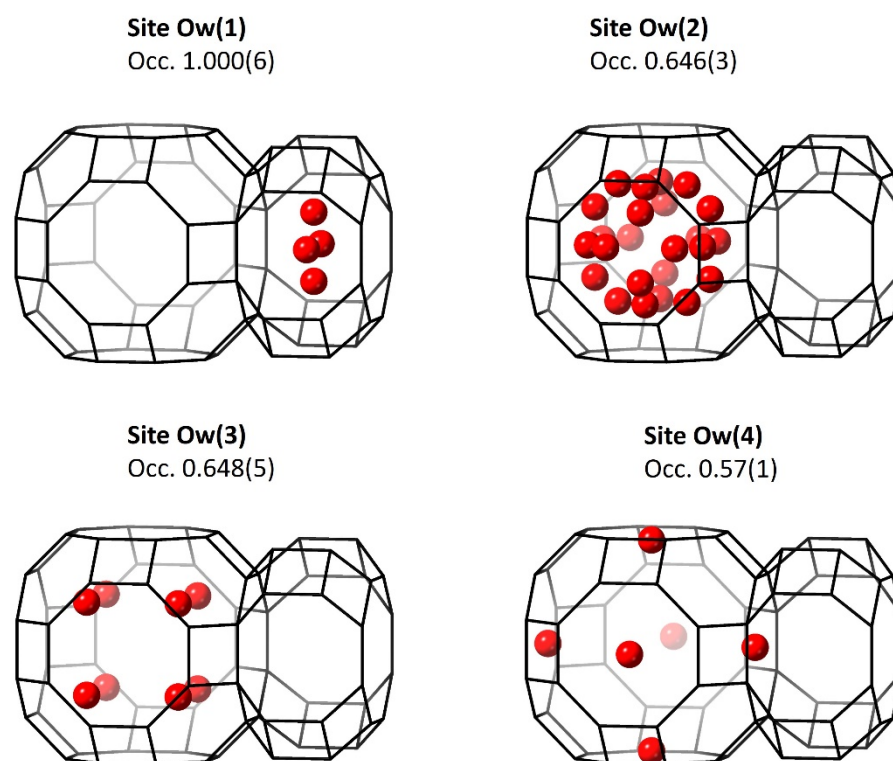**Figure 6.** Location of the K(1)–K(3) cations sites determined in the empty zeolite ZK-5. The framework is shown as a stick model and the potassium cations as purple spheres. The fractional occupancy (Occ.) of each site is also included.

Sites K(1) and K(3) are still observed in the filled zeolite ZK-5 structure, with the former retaining its 100% occupancy. However, there is a significant reduction in the occupancy of site K(3), and an equivalent K(2) in the α-cage is no longer observed. Instead, there has been the introduction of a new K(4) site at the centre of the α-cage, which is associated with the occluded 18C6 species. The K(4) site will be discussed further alongside the crystallographic sites of the 18C6 oxyethylene chain.

### 3.3.2. Water Molecules

As the zeolite ZK-5 samples were hydrated when analysed, crystallographic sites for the oxygen atoms in extra-framework water molecules (Ow) were determined. In the empty zeolite four water molecule sites were observed, as shown in Figure 7. Site Ow(1) is positioned within the *t-pau* unit, adjacent to site K(1) and separated by an interatomic distance of 2.93 Å. According to Gagné and Hawthorne [47] this is within the range of expected K-O bond distances, suggesting that site Ow(1) water molecules are coordinated to site K(1) cations. In the empty zeolite ZK-5 site Ow(1) has an occupancy of 1.000(6), indicating that every K(1) cation would be hydrated by an Ow(1) water molecule. However, in the filled structure the Ow(1) occupancy is reduced to 0.866(9). Furthermore, the distance between site Ow(1) and K(3) is 3.16 Å, which in line with the expected distances, suggests that K(3) cations are also coordinated to site Ow(1) water molecules.

**Site Ow(1)**
Occ. 1.000(6)

**Site Ow(2)**
Occ. 0.646(3)

**Site Ow(3)**
Occ. 0.648(5)

**Site Ow(4)**
Occ. 0.57(1)

**Figure 7.** Location of the Ow(1)-Ow(4) water molecule oxygen sites determined in the empty zeolite ZK-5. The framework is shown as a stick model and the water oxygen sites as red spheres. Included is the fractional occupancy (Occ.) of each site.

The three remaining Ow sites are all positioned within the α-cage. The Ow(2) site is represented by a cluster in a truncated octahedron arrangement, with the single four-rings being parallel to the eight-ring apertures of the α-cage. In the empty zeolite ZK-5 structure this site has an occupancy of 0.352(5), averaging at 2.8 Ow(2) water molecules per α-cage. Site Ow(2) is expected to be coordinated to site K(2) cations, with an interatomic distance of 3.15 Å. In contrast, the distance between site Ow(2) and K(3) is greater at 3.85 Å, suggesting coordination between the two is unlikely. The Ow(2) site is not observed in the filled zeolite ZK-5 structure. Moreover, excluding the K(4) site associated with the 18C6, it should be noted that these models indicate that all the K$^+$ cation sites are potentially hydrated by a water molecule.

Site Ow(3) is adjacent to the S6R faces, exhibiting overlap with the K(2) site, as shown in the average unit cell structure in Figure S5 in the SI. In the empty zeolite structure, the occupancy of site Ow(3) is 0.648(5), indicating that the position adjacent to the S6R faces is either occupied by a Ow(3) water molecule (65%) or a K(2) cation (35%). Following the absence of site K(2) in the filled zeolite structure, the occupancy of the Ow(3) site is

1.00(2). The final water molecule site is Ow(4), positioned within the $\alpha$-cage, adjacent to the S8R apertures. The occupancy is reported as 0.57(1) and 0.96(1) for the empty and filled structures, respectively. Significant distinctions in the $\alpha$-cage water molecules occupancies between the empty and filled zeolites are expected due to the presence of the 18C6 species within the framework cavity.

### 3.3.3. 18C6 Species

As with zeolite RHO, the occluded 18C6 was modelled as a rigid body within the zeolite ZK-5 framework, being seen to occupy the $\alpha$-cage as predicted [33,34]. The atomic sites of the 18C6 species within the zeolite ZK-5 $\alpha$-cage are shown in Figure 8. In this case, during refinement a $K^+$ cation was observed to occupy the centre of the 18C6 cavity, being the K(4) site. This demonstrates that the occluded 18C6 species exists as a ((18C6)$K^+$) macrocation in the $\alpha$-cage, and is anticipated to be the identity of the organic additive involved in the framework assembly. This is analogous to **FAU** and **EMT**-type zeolites where the ((18C6)$Na^+$) macrocation exists within the framework supercages [29].
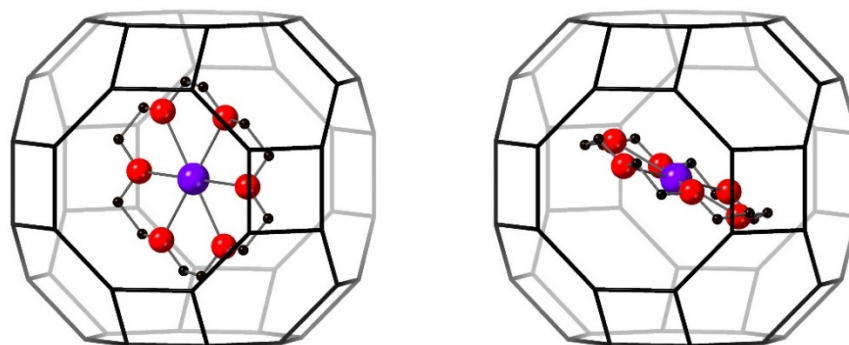


**Figure 8.** Location of the C and O sites of the 18C6 oxyethylene chain in the $\alpha$-cage of the filled zeolite ZK-5. Included is the position of the K(4) cation site, as shown by a purple sphere. An example of two 18C6 orientations in the cage are shown. The framework is shown as a stick model, the carbon sites as black spheres and the oxygen sites as red spheres.

In further congruence with zeolite RHO, due to the cubic symmetry each C and O site expresses a multiplicity of 48 and 24 within the unit cell and $\alpha$-cage, respectively. Again, the occupancy of the C and O sites were constrained to be equivalent, giving an occupancy of 0.0276(2) to the oxyethylene chain. Therefore, it is estimated that there are 0.66 18C6 species per $\alpha$-cage and 1.3 per unit cell, which also agrees with the calculations from the thermogravimetric analysis. Furthermore, the occupancy of site K(4) was not constrained alongside the oxyethylene sites, and was refined to 0.653(9). This is in further agreement with the estimated number of 18C6 species per $\alpha$-cage, and supports that the occluded 18C6 species exists as a ((18C6)$K^+$) macrocation. As with zeolite RHO, the inherent cubic symmetry results in several orientations of the 18C6 species (Figure 8), with no periodic ordering.

It is suspected that the occluded 18C6 species being a ((18C6)$K^+$) macrocation explains the differences in both cation and water site occupancies between the filled and empty zeolite ZK-5 structures. The presence of the macrocation in the filled zeolite must be sufficient to screen the framework's anionic charge within the $\alpha$-cage, such that the K(2) site is not necessary. As a consequence, the site adjacent to the S6R faces is instead fully occupied by the Ow(3) water molecule sites in the filled zeolite, and hydrates the ((18C6)$K^+$) macrocation. Upon calcination and removal of the 18C6 to prepare the empty analogue, there must be a sequential redistribution of $K^+$ cations to retain the material's net neutrality. Therefore, it is proposed that the cations in site K(4) migrate to sites K(2) and K(3) in the empty zeolite ZK-5. Furthermore, following the removal of 18C6, water molecule site Ow(2) is introduced to occupy the void space in the $\alpha$-cage and hydrate the K(2) site.

It should also be noted that the isotropic displacement parameters for the C and O sites of the 18C6 oxyethylene chain in zeolite ZK-5 are significantly greater than those refined for zeolite RHO. This indicates greater displacement is observed for the occluded 18C6 species in the former, which can be attributed to the sample being scanned at ambient temperature, as opposed to 100 K for latter.

## 4. Discussion

In zeolites RHO and ZK-5 it is seen that the occluded 18C6 species occupies the $\alpha$-cage, as has been expected [33,34] but not explicitly proven. In both zeolites the 18C6 species is disordered amongst several possible orientations due to the inherent symmetry of the cubic system, whereby all three crystallographic axes are indistinguishable. Consequently, the periodic structure is an average of all these possible permutations, producing the average structure reported herein. The observation that the occluded 18C6 species fails to match up with the framework symmetry, as seen in zeolite EMC-2 [29], would suggest that the 18C6 species does not behave as a geometric template in the crystallisation of zeolites RHO and ZK-5. However, as both the 18C6 molecule in the $D_{3d}$ conformation and the $\alpha$-cage S6R faces share three-fold symmetry, we speculate that the 18C6 species may adsorb to these faces on the crystal surface, promoting the growth of an adjacent $\alpha$-cage. Crystal growth along this (111) direction would consequently lead to cubic close packing of the $\alpha$-cages.

Interestingly, both zeolites RHO and ZK-5 can be prepared without the need for 18C6, [27,51–53] in contrast to zeolite EMC-2 where it appears to be a necessity [20,28]. For zeolite RHO it is the $Cs^+$ cations that direct the assembly of the D8Rs [54] and in zeolite ZK-5 the $K^+$ cations are involved in the formation of the t-pau units [48]. In both cases, this behaviour must be sufficient to assemble the relevant framework structure, without the need for an organic additive. Instead, it is expected that the 18C6 influences the kinetics of crystallisation. We believe that the 18C6 species must play a role as a space-filling species that stabilises the formation of the $\alpha$-cage, which is supported by its presence in this cavity in both crystal structures. For zeolite RHO it is the non-complexed 18C6 molecule and in zeolite ZK-5 it is the $((18C6)K^+)$ macrocation that performs this stabilisation role. In both cases, the stabilising would involve non-bonding van der Waals interactions with the growing framework, with the $((18C6)K^+)$ macrocation having the addition of electrostatic interactions for zeolite ZK-5. The influence of this stabilisation on the actual synthesis of zeolite RHO is that it becomes increasingly facile and expands the crystallisation field [55–58] Therefore, we anticipate a similar impact on the synthesis of zeolite ZK-5. Such behaviour would suggest that it influences the free-energy of crystallisation, as we have seen for **FAU** and **EMT**-type zeolites [20].

## 5. Conclusions

Herein, we present the crystal structure of the as-synthesised, 18C6-containing and calcined analogues of zeolites RHO and ZK-5. We have successfully elucidated the identity of the occluded 18C6 species, which in zeolite RHO is an isolated 18C6 molecule, and in zeolite ZK-5 is a coordinated $((18C6)K^+)$ macrocation. In both zeolites, we observe that the relevant 18C6 species occupies the $\alpha$-cage cavities. According to the fractional occupancies and thermogravimetric data, we predict that there are 0.54 molecules per cage in the former, and 0.66 macrocations per cage in the latter. Furthermore, the occluded 18C6 species can be present in a number of different orientations, with no periodic ordering between adjacent unit cells. The structures observed are thus an average of the available permutations.

Due to the lack of symmetry matchup between the 18C6 species and the zeolite framework it is deemed that in both cases the relevant 18C6 species does not behave as a true geometric template. Instead, we believe that the role of the 18C6 species is better described as a structure directing or space-filling agent. Rather than imprinting symmetry during crystallisation, the 18C6 species stabilise the open void of the $\alpha$-cage as it is being assembled.

Using these crystal structures, a more coherent understanding of the role of 18C6 as an organic additive in the synthesis of zeolites can be reached. This presents the need for greater appreciation of the multiple available behaviours of organic additives that can be applied to prepare new zeolites.

## References

1. Barrer, R.M. *Hydrothermal Chemistry of Zeolites*; United States Edition ed.; Academic Press Inc. Ltd.: New York, NY, USA, 1982.
2. Jacobs, P.A.; Flanigen, E.M.; Jansen, J.C.; van Bekkum, H. *Introduction to Zeolite Science and Practice*, 2nd ed.; Elsevier Science: Amsterdam, The Netherlands, 2010.
3. Ipek, B.; Altiparmak, I. Remarkable isosteric heat of hydrogen adsorption on Cu(I)-exchanged SSZ-39. *Int. J. Hydrog. Energy* **2020**, *45*, 34972–34982. [CrossRef]
4. Fisher, J.C.; Siriwardane, R.V.; Stevens, R.W., Jr. Zeolite-based process for $CO_2$ capture from high-pressure, moderate-temperature gas streams. *Ind. Eng. Chem. Res.* **2011**, *50*, 13962–13968. [CrossRef]
5. Dyer, A.; Hriljac, J.; Evans, N.; Stokes, I.; Rand, P.; Kellet, S.; Harjula, R.; Moller, T.; Maher, Z.; Heatlie-Branson, R.; et al. The use of columns of the zeolite clinoptilolite in the remediation of aqueous nuclear waste streams. *J. Radioanal. Nucl. Chem.* **2018**, *318*, 2473–2491. [CrossRef] [PubMed]
6. Moore, P.B.; Smith, J.V. Archimedean polyhedra as the basis of tetrahedrally-coordinated frameworks. *Mineral. Mag. J. Mineral. Soc.* **1964**, *33*, 1008–1014. [CrossRef]
7. Wilson, S.T. Templating in molecular sieve synthesis. In *Verified Syntheses of Zeolitic Materials*; Elsevier: Amsterdam, The Netherlands, 2001; pp. 27–31.
8. Cundy, C.S.; Cox, P.A. The hydrothermal synthesis of zeolites: Precursors, intermediates and reaction mechanism. *Microporous Mesoporous Mater.* **2005**, *82*, 1–78. [CrossRef]
9. Brunner, G. A proposal for a mechanism of nucleation in zeolite synthesis. *Zeolites* **1992**, *12*, 428–430. [CrossRef]
10. Burkett, S.L.; Davis, M.E. Mechanism of structure direction in the synthesis of pure-silica zeolites. 2. Hydrophobic hydration and structural specificity. *Chem. Mater.* **1995**, *7*, 1453–1463. [CrossRef]
11. Burkett, S.L.; Davis, M.E. Mechanisms of structure direction in the synthesis of pure-silica zeolites. 1. Synthesis of TPA/Si-ZSM-5. *Chem. Mater.* **1995**, *7*, 920–928. [CrossRef]

12. Flanigen, E.M.; Bennett, J.; Grose, R.; Cohen, J.; Patton, R.; Kirchner, R.; Smith, J. Silicalite, a new hydrophobic crystalline silica molecular sieve. *Nature* **1978**, *271*, 512–516. [CrossRef]

13. Oleksiak, M.D.; Rimer, J.D. Synthesis of zeolites in the absence of organic structure-directing agents: Factors governing crystal selection and polymorphism. *Rev. Chem. Eng.* **2014**, *30*, 1–49. [CrossRef]

14. Baerlocher, C.; McCusker, L.B. Database of Zeolite Structures. Available online: http://www.iza-structure.org/databases/ (accessed on 9 January 2016).

15. Lobo, R.F.; Zones, S.I.; Davis, M.E. Structure-direction in zeolite synthesis. *Incl. Chem. Zeolites Nanoscale Mater. Des.* **1995**, *21*, 47–78.

16. Davis, M.E.; Lobo, R.F. Zeolite and molecular sieve synthesis. *Chem. Mater.* **1992**, *4*, 756–768. [CrossRef]

17. Cox, P.A.; Casci, J.L.; Stevens, A. Molecular modelling of templated zeolite synthesis. *Faraday Discuss.* **1997**, *106*, 473–487. [CrossRef]

18. Zones, S.I.; Nakagawa, Y. Boron-beta zeolite hydrothermal conversions: The influence of template structure and of boron concentration and source. *Microporous Mater.* **1994**, *2*, 543–555. [CrossRef]

19. Fletcher, R.E.; Wells, S.A.; Leung, K.M.; Edwards, P.P.; Sartbaeva, A. Intrinsic flexibility of porous materials; theory, modelling and the flexibility window of the EMT zeolite framework. *Acta Crystallogr. Sect. B Struct. Sci. Cryst. Eng. Mater.* **2015**, *71*, 641–647. [CrossRef] [PubMed]

20. Nearchou, A.; Cornelius, M.-L.U.; Skelton, J.M.; Jones, Z.L.; Cairns, A.B.; Collings, I.E.; Raithby, P.R.; Wells, S.A.; Sartbaeva, A. Intrinsic flexibility of the EMT zeolite framework under pressure. *Molecules* **2019**, *24*, 641. [CrossRef] [PubMed]

21. Stevens, A.P.; Gorman, A.M.; Freeman, C.M.; Cox, P.A. Prediction of template location via a combined Monte Carlo–simulated annealing approach. *J. Chem. Soc. Faraday Trans.* **1996**, *92*, 2065–2073. [CrossRef]

22. Lewis, D.W.; Willock, D.J.; Catlow, C.R.A.; Thomas, J.M.; Hutchings, G.J. De novo design of structure-directing agents for the synthesis of microporous solids. *Nature* **1996**, *382*, 604–606. [CrossRef]

23. Lewis, D.W.; Freeman, C.M.; Catlow, C.R.A. Predicting the templating ability of organic additives for the synthesis of microporous materials. *J. Phys. Chem.* **1995**, *99*, 11194–11202. [CrossRef]

24. Chatelain, T.; Patarin, J.; Farre, R.; Petigny, O.; Schulz, P. Synthesis and characterization of 18-crown-6 ether-containing KFI-type zeolite. *Zeolites* **1996**, *17*, 328–333. [CrossRef]

25. Chatelain, T.; Patarin, J.; Soulard, M.; Guth, J.L.; Schulz, P. Synthesis and characterization of high-silica EMT and FAU zeolites prepared in the presence of crown-ethers with either ethylene-glycol or 1,3,5-trioxane. *Zeolites* **1995**, *15*, 90–96. [CrossRef]

26. Chatelain, T.; Patarin, J.; Fousson, E.; Soulard, M.; Guth, J.L.; Schulz, P. Synthesis and characterization of high-silica zeolite-rho prepared in the presence of 18-crown-6 ether as organic template. *Microporous Mater.* **1995**, *4*, 231–238. [CrossRef]

27. Robson, H. *Verified Syntheses of Zeolitic Materials*; Second Revised Edition ed.; Elsevier Science, B.V.: Amsterdam, The Netherlands, 2001; p. 265.

28. Nearchou, A.; Raithby, P.R.; Sartbaeva, A. Systematic approaches towards template-free synthesis of EMT-type zeolites. *Microporous Mesoporous Mater.* **2018**, *255*, 261–270. [CrossRef]

29. Baerlocher, C.; McCusker, L.B.; Chiappetta, R. Location of the 18-crown-6 template in EMC-2 (EMT) Rietveld refinement of the calcined and as-synthesised forms. *Microporous Mater.* **1994**, *2*, 269–280. [CrossRef]

30. Terasaki, O.; Ohsuna, T.; Alfredsson, V.; Bovin, J.O.; Watanabe, D.; Carr, S.W.; Anderson, M.W. Observation of spatially correlated intergrowths of faujastic polytypes and the pure end members by high-resolution electron microscopy. *Chem. Mater.* **1993**, *5*, 452–458. [CrossRef]

31. Ohsuna, T.; Terasaki, O.; Alfredsson, V.; Bovin, J.O.; Watanabe, D.; Carr, S.W.; Anderson, M.W. Observations on the role of crown ether templates in the formation of hexagonal and cubic polymorphs of zeolite Y. *Proc. R. Soc. A-Math. Phys. Eng. Sci.* **1996**, *452*, 715–740.

32. Burkett, S.L.; Davis, M.E. Structure-directing effects in the crown ether-mediated synthesis of FAU and EMT zeolites. *Microporous Mater.* **1993**, *1*, 265–282. [CrossRef]

33. Nearchou, A.; Armstrong, J.; Butler, K.T.; Raithby, P.R.; Sartbaeva, A. Differentiating the role of organic additives to assemble open framework aluminosilicates using INS spectroscopy. *Phys. Chem. Chem. Phys.* **2020**, *22*, 14177–14186. [CrossRef]

34. Chatelain, T.; Patarin, J.; Brendle, E.; Dougnier, F.; Guth, J.L.; Schulz, P. Synthesis of high-silica FAU-, EMT-, RHO- and KFI-type zeolites in the presence of 18-crown-6 ether. *Stud. Surf. Sci. Catal.* **1997**, *105*, 173–180.

35. Lippmaa, E.; Maegi, M.; Samoson, A.; Tarmak, M.; Engelhardt, G. Investigation of the structure of zeolites by solid-state high-resolution silicon-29 NMR spectroscopy. *J. Am. Chem. Soc.* **1981**, *103*, 4992–4996. [CrossRef]

36. Coelho, A.A. TOPAS and TOPAS-Academic: An optimization program integrating computer algebra and crystallographic objects written in C++. *J. Appl. Crystallogr.* **2018**, *51*, 210–218. [CrossRef]

37. Parise, J.B.; Cox, D.E. Structural changes occurring upon dehydration of zeolite Rho. A study using neutron powder diffraction and distance-least-squares structural modeling. *J. Phys. Chem.* **1984**, *88*, 1635–1640. [CrossRef]

38. Parise, J.B.; Shannon, R.D.; Prince, E.; Cox, D. The crystal structures of the synthetic zeolites (Cs, K)-ZK5 and (Cs, D)-ZK5 determined from neutron powder diffraction data. *Z. Für Krist.-Cryst. Mater.* **1983**, *165*, 175–190. [CrossRef]

39. Toby, B.H. R factors in Rietveld analysis: How good is good enough? *Powder Diffr.* **2006**, *21*, 67–70. [CrossRef]

40. Merritt, E.A. Some $B_{eq}$ are more equivalent than others. *Acta Crystallogr. Sect. A Found. Crystallogr.* **2011**, *67*, 512–516. [CrossRef] [PubMed]

41. Nearchou, A.; Castaing, R.; Raithby, P.R.; Sartbaeva, A. Zeolites fit for a crown: Studying organic-framework host-guest interactions through thermogravimetric techniques. *Microporous Mesoporous Mater.* **2020**, *308*, 110479. [CrossRef]

42. Baerlocher, C.; McCusker, L.B.; Olson, D.H. *Atlas of Zeolite Framework Types*, 6th ed.; Elsevier: Amsterdam, The Netherlands, 2007; p. 405.

43. Robson, H.E.; Shoemaker, D.P.; Ogilvie, R.A.; Manor, P.C. Synthesis and crystal-structure of zeolite Rho—A new zeolite related to Linde Type-A. *Adv. Chem. Ser.* **1973**, *121*, 106–115.

44. Parise, J.B.; Gier, T.E.; Corbin, D.R.; Abrams, L.; Jorgensen, J.D.; Prince, E. Flexibility of the framework of zeolite Rho. Structural variation from 11 to 573 K. A study using neutron powder diffraction data. *J. Phys. Chem.* **1984**, *88*, 2303–2307. [CrossRef]

45. Nearchou, A.; Cornelius, M.-L.U.; Jones, Z.L.; Collings, I.E.; Wells, S.A.; Raithby, P.R.; Sartbaeva, A. Pressure-Induced Symmetry Changes in Body-Centered Cubic Zeolites. *R. Soc. Open Sci.* **2019**, *6*, 182158. [CrossRef] [PubMed]

46. Lee, Y.; Hriljac, J.A.; Vogt, T.; Parise, J.B.; Edmondson, M.J.; Anderson, P.A.; Corbin, D.R.; Nagai, T. Phase transition of zeolite RHO at high-pressure. *J. Am. Chem. Soc.* **2001**, *123*, 8418–8419. [CrossRef] [PubMed]

47. Gagné, O.C.; Hawthorne, F.C. Bond-length distributions for ions bonded to oxygen: Alkali and alkaline-earth metals. *Acta Crystallogr. Sect. B Struct. Sci. Cryst. Eng. Mater.* **2016**, *72*, 602–625. [CrossRef] [PubMed]

48. Meier, W.M.; Kokotailo, G.T. The crystal structure of synthetic zeolite ZK-5. *Z. Krist.-Cryst. Mater.* **1965**, *121*, 211–219. [CrossRef]

49. Lievens, J.L.; Verduijn, J.P.; Mortier, W.J. Cation site energies in dehydrated KFI-type zeolites: D-NaKFI, d-NaHKFI, and d-KKFI. *Zeolites* **1992**, *12*, 690–697. [CrossRef]

50. Treacy, M.M.; Higgins, J.B. *Collection of Simulated XRD Powder Patterns for Zeolites*; 5th ed.; Elsevier: Amsterdam, The Netherlands, 2007.

51. Nearchou, A.; Sartbaeva, A. Influence of alkali metal cations on the formation of zeolites under hydrothermal conditions with no organic structure directing agents. *Crystengcomm* **2015**, *17*, 2496–2503. [CrossRef]

52. Robson, H.E. Method for Preparing a Small Pore Synthetic Zeolite. U.S. Patent 3,720,753, 13 March 1973.

53. Verduijn, J.P. Zeolite ZK-5. U.S. Patent 4,994,249, 19 February 1991.

54. Liu, S.; Zhang, P.; Meng, X.; Liang, D.; Xiao, N.; Xiao, F.-S. Cesium-free synthesis of aluminosilicate RHO zeolite in the presence of cationic polymer. *Microporous Mesoporous Mater.* **2010**, *132*, 352–356. [CrossRef]

55. McCusker, L.B.; Baerlocher, C. *The Sixth International Zeolite Conference*; Butterworths: Guildford, UK, 1983; p. 812.

56. Barrer, R.M.; Barri, S.; Klinowski, J. Proceedings of the Fifth International Zeolite Conference, Heyden, London, 2–6 June 1980; p. 20.

57. Araki, S.; Kiyohara, Y.; Tanaka, S.; Miyake, Y. Adsorption of carbon dioxide and nitrogen on zeolite rho prepared by hydrothermal synthesis using 18-crown-6 ether. *J. Colloid Interface Sci.* **2012**, *388*, 185–190. [CrossRef] [PubMed]

58. Araki, S.; Kiyohara, Y.; Tanaka, S.; Miyake, Y. Crystallization process of zeolite rho prepared by hydrothermal synthesis using 18-crown-6 ether as organic template. *J. Colloid Interface Sci.* **2012**, *376*, 28–33. [CrossRef] [PubMed]

59. Galli, E.; Gottardi, G.; Pongiluppi, D. The crystal structure of the zeolite merlinoite. *Neues Jahrb. Mineral. Mon.* **1979**, 1–9.